Post-Print

R.J. Ferreira, A.M. Grande, J.M. Guedes, A.M. Deus, G. Sala
Combination of Topology and Shape Optimization with Finite Element Modeling in the Case of an Aerospace Component Produced by Laser Based Additive Manufacturing
Journal of Laser Applications, Vol. 35, N. 2, 2023, 022031 (17 pages)
doi:10.2351/7.0000919

The following article appeared in Journal of Laser Applications, Vol. 35, N. 2, 2023, 022031 and may be found at: https://doi.org/10.2351/7.0000919

ACKNOWLEDGEMENT
This project has received funding from the Clean Sky 2 Joint Undertaking (JU) under grant agreement No 717194. The JU receives support from the European Union's Horizon 2020 research and innovation programme and the Clean Sky 2 JU members other than the Union.

Combination of Topology and Shape Optimization with Finite Element Modeling in the Case of an Aerospace Component Produced by Laser Based Additive Manufacturing

R.J. Ferreira,[1,2] A.M. Grande,[2,*] J.M. Guedes,[1,3] A.M. Deus,[4,5] and G. Sala[2]
[1)]*Departamento de Engenharia Mecânica, Instituto Superior Técnico, Universidade de Lisboa, Lisboa, Portugal*
[2)]*Department of Aerospace Science and Technology, Politecnico di Milano, Milano, Italy*
[3)]*IDMEC, Instituto Superior Técnico, Universidade de Lisboa, Lisboa, Portugal*
[4)]*Departamento de Engenharia Mecânica, Instituto Superior Técnico, Universidade de Lisboa, Lisboa, Portugal*
[5)]*CeFEMA, Instituto Superior Técnico, Universidade de Lisboa, Lisboa, Portugal*

(*Corresponding author: antoniomattia.grande@polimi.it.)

(Dated: 10 April 2023)

The present work applies a Design for Additive Manufacturing (DfAM) driven design methodology to an aeronautical component, to be fabricated through an Additive Manufacturing (AM) process. This involves simulation of the process using Abaqus Finite Element software, as well as the development of a design methodology concerning topology and shape optimization, utilizing SIMULIA Tosca. A benchmarking AM simulation is performed first to provide validation and general guidelines needed to properly implement a low-resolution AM simulation in Abaqus. The structural optimization is started by a volume minimization topology optimization. Solid Isotropic Material with Penalization (SIMP) fails to achieve convergence with frequency response constraints, while Mass Interpolation Material Penalization (MIMP) converges to a well-connected design. The design interpretation with polyNURBs results in a single component with a weight reduction of 2.29% compared to the current two component assembly. Further implementation of a shape optimization to address stress design requirements allows achieving stress homogeneity and a lower weight, resulting in a 5.12% weight reduction. The AM simulation process is applied to a scaled version of the final design, to both assess the printability of the part itself, as well as the implementation of the key tools to define the AM simulation. Maximum distortion of the part appears at expected regions, with overhanging material.

Keywords: Topology Optimization, Shape Optimization, SIMP/MIMP, Finite Element Method, Laser Additive Manufacturing, Residual Stress.

ACRONYMS

AM: Additive Manufacturing

AMATHO: Additive MAnufacturing Tilt-rotor HOusing

CAD: Computer Aided Design

CAM: Computer Aided Modeling

DfAM: Design for Additive Manufacturing

FE: Finite Element

FEA: Finite Element Analysis

FEM: Finite Element Modeling

MIMP: Mass Interpolation Material Penalization

NGCTR: Next Generation Civil Tilt-rotor

NIST: National Institute of Standards and Technology

PEDE: Niels-Pedersen Approach

SIMP: Solid Isotropic Material with Penalization

SLM: Selective Laser Melting

SO: Shape Optimization

TO: Topology Optimization

I. INTRODUCTION

Additive Manufacturing (AM) has received considerable attention in the past two decades, although it had been present quite earlier, e.g. in the procedures to construct free-form topographical maps and photo-sculptures with 2D layers[1–3] even more than a century ago. In the 1960s, with the advent of Computer Aided Design (CAD) and Manufacturing (CAM), with processes such as powder fusion[4], photopolymerization[5], and sheet lamination[6], the groundwork for the modern AM processes[7] was set. Nowadays, AM processes are present in a wide range of sectors, like medical, space, and aeronautical[7].

The wide usage of AM technologies relies on a set of advantages it provides over conventional manufacturing technologies (e.g. milling, drilling, or casting). It allows for increased geometrical complexity, especially important during light-weighting processes; a reduction of material waste due to the additive nature of the processes; and high customization, which allows for specialized, on-demand, printed parts. However, AM is not the choice for many applications, due to its drawbacks and unsolved problems[8]. These are, for instance, the build size limitations, constrained by the dimensions of the build chamber or low deposition rates; the production and hardware costs, which are higher than conventional manufacturing methods as the production scale increases;

anisotropic mechanical performance due to the layer-by-layer manufacturing; post-printing part distortion and cracking; and process complexity reliant on many parameters that impact the final part quality and mechanical performance.

Selective Laser Melting (SLM) is one of the most common AM processes and is featured in the current work. It involves the operation of a laser that selectively fuses layers of a powdered material along a predefined trajectory. As such, it is a powder-bed based AM technology, that allows the production of a part with a fine microstructure, and similar properties to the ones obtained from conventional methods. However, the process parameters such as power, scanning speed, beam diameter, or cooling times, are tightly interconnected, and thus heavily influence the quality of the printed part[9].

In order to maximize the quality of parts produced, a set of guidelines and a structured framework are necessary. These are conventionally named Design for Additive Manufacturing (DfAM) guidelines, and focus on the printing steps of a part, be it during its design and conceptualization stage, the printing process itself, or the post-processing procedures (e.g. support removal and heat treatments). The present work focuses on the application of structural optimization and lightweighting techniques, given the ability of AM technologies to print highly complex structures. Topology optimization (first introduced by Bendsøe and Kikuchi in 1988[10]) is the main optimization tool utilized. It allows to further include AM specific considerations (constraints) that impact a part's performance and printability. These DfAM constraints can be subdivided into so-called directional and non-directional categories. The first set are directly influenced by the print direction and includes anisotropy, support structures design and optimization, and the presence of distortion and residual stresses. The non-directional constraints are not influenced by the build direction, and include power enclosure, and feature size control. To achieve a more complete implementation of the DfAM guidelines, all constraints should be considered and implemented during the topology optimization designing phase. However, considering the application of the methodology in the context of the present work, with relevance to the aeronautical sector, where maximum weight reduction is sought-after, support structure optimization and anisotropy considerations are not included in the present formulation.

Alongside the structural optimization procedure, modeling of distortion and residual stress prediction is important, in order to achieve good quality in printing, and to better understand and optimize the parameters that control the printing process[8]. As such, a numerical AM process simulation finite element (FE) model is developed and applied to a highly complex geometry, based on an uncoupled thermal-mechanical procedure, providing an extra design validation step.

A more comprehensive description of the current work can be found elsewhere[11].

A. AMATHO

The AMATHO project (Additive MAnufacturing Tilt-rotor HOusing) tackles directly the first goal set by Clear Sky 2, the European Union initiative for sustainable aviation. By taking advantage of the Additive Manufacturing potential, it aims at the design and manufacture of a gearbox housing to be utilized by Leonardo Helicopter's Next Generation Civil Tilt-rotor (NGCTR). The integration of AM in the design process allows for reduced weight and optimized performance, saving resources during both manufacturing and flight time.

B. Problem definition

The target problem of the present work is the optimum design of an aeronautical component to be employed by Leonardo Helicopters, utilizing SLM as the AM process.

The currently used component assembly is made of two individual parts and it can be seen in figure 1, highlighting an upper and lower manifold.

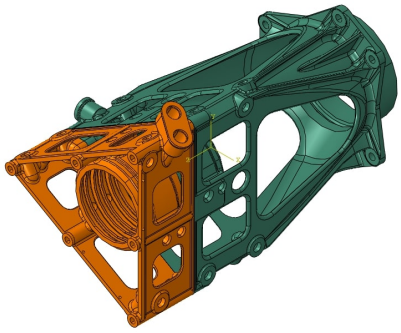

FIG. 1. Current component containing the upper manifold (green), and lower manifold (orange).

Three servo-actuators are connected to the part through eighteen mounting bosses, six on each of the three faces. Both the load application points (AF_{Si}) and servo-actuators centers of mass (CG_i) are provided. Static strength of the component is defined under two loading conditions (axial and bending), and three load intensities for each. Under proof stress loading intensity, the part shall not experience any yielding. While not directly assessed in this work, fatigue loading is also used to justify the definition of two additional bending load cases, in order to achieve topology optimization solution symmetry. The servo-actuator is subjected to a minimum axial stiffness requirement in the z-direction, whereas the mounting bosses themselves are subjected to both a relative and normal stiffness requirement. Finally, a minimum first natural frequency is also defined.

C. Design process approach

To the above-mentioned problem, a DfAM guided approach is employed to obtain a design compliant with the requirements defined by Leonardo Helicopters, with the goal of obtaining a matching or preferably lower weight, as compared to the currently used design. Firstly, a topology optimization

task is carried out, based on the limiting geometry, design requirements, and loading conditions. The interpretation of the results is carried out by using polyNURBs in Altair Inspire. Following the design interpretation, such part is subjected to the same loading conditions and modal analysis to verify the compliance with the constraints. If the result is not satisfactory, the topology optimization parameters are adjusted, until a design is chosen. Such resulting part is then subjected to a shape optimization procedure to address the static strength requirements and obtain stress homogeneity (with added durability in the case of fatigue loading). Identically, the shape optimization process is carried out until a satisfactory result is obtained, and could be comprised of several iterations, with the goal of minimizing stress peaks, thus extending fatigue life of the part. Finally, a thermo-mechanical FE simulation is carried out to highlight the part's performance under the complex thermal-mechanical process it undergoes, namely regarding distortion and residual stresses. Figure 2 is the proposed design workflow for this project.

II. STRUCTURAL OPTIMIZATION FORMULATION

Structural optimization has the objective of finding the best way an assembly of materials may be set, to withstand a set of loading and boundary conditions. However, the definition of goal may vary, depending on the project's objectives. As an example, one may seek a minimum weight approach. Therefore, the definition of the structural optimization problem involves the search of the assembly of material that, while respecting a given set of requirements (stiffness, weight, eigenvalues, displacement, etc.), optimally sets the objective of interest, that could be, for example, the stiffness or weight of said structure.

A general structural optimization problem is defined by an objective function ($f(x,y)$, representing the objective to be optimized), a design variable (x, which describes the design, and is typically the geometry of the structure), and the state variable ($y(x)$, which represents the structure's response for a given design variable).

A. General topology optimization formulation

Most commercially available FEA software that support topology optimization, utilize a density-based approach, namely through the use of the Solid Isotropic Material with Penalization (SIMP) interpolation method[12]. Consider a minimum compliance problem for a generic continuum structure, defined as,

$$\begin{cases} \min\limits_{\boldsymbol{u},\boldsymbol{E_e}} \boldsymbol{f}^T\boldsymbol{u} \\ s.t. \begin{cases} \boldsymbol{K}(E_e)\boldsymbol{u} = \boldsymbol{f} \\ E_e \in E_{adm} \end{cases} \end{cases}, \tag{1}$$

where $\boldsymbol{f}$ and $\boldsymbol{u}$ represent the load and displacement vectors, respectively, and E_{adm} represents the admissible stiffness tensors.

In order to obtain a design with well-defined voids and solid regions (1-0 design), intermediate density values are to be steered towards the two extremes. This is achieved through the use of interpolation methods, with the most commonly used being the SIMP method. However, SIMULIA's recently introduced Mass Interpolation Material Penalization (MIMP) method[13] is of interest for the problem at hands and is implemented in this work.

B. Solid isotropic material with penalization

Originally developed by Rozvany, et al., 1992[14], based on the approach introduced by Bendsøe & Sigmund, 2003[12], SIMP is simply defined by a penalization factor p, which penalizes intermediate densities to the bounds of the interval $\rho \in [\rho_{min}, 1]$, such that,

$$E_{ijkl}(\boldsymbol{x}) = \rho(\boldsymbol{x})^p E^0_{ijkl}, \quad p > 1. \tag{2}$$

C. Mass interpolation material penalization

The MIMP algorithm is based on a combination between SIMP for the constitutive material interpolation, and a SIMULIA developed physical density material interpolation. Its suggested use is in strength optimization with applied stress, either as an objective, or as a constraint. Additionally, it reportedly improves results with mass-related responses, such as natural frequency, since previously the algorithm would by default change the interpolation scheme to PEDE (the so-called Niels-Pedersen based approach, also proprietary to SIMULIA[15]).

D. Volume minimization problem

The volume minimization procedure is another possible approach to topology optimization, in contrast to the typically used minimum compliance with volume constraint problem. Additional constraints must be defined to ensure the design is not completely void ($\rho_e = \rho_{min}, \forall e = 1,\ldots,N_e$). These constraints can be placed on the displacement or frequency response of the structure. The formulation of the problem is defined by,

$$\begin{cases} \min\limits_{\rho_e} \varphi(\boldsymbol{\rho}) = \sum\limits_{e=1}^{N} \rho_e v_e \\ s.t. \begin{cases} \boldsymbol{K}(E_e)\boldsymbol{u} = \boldsymbol{f} \\ u(\boldsymbol{\rho}) \leq \bar{u} \\ 0 < \rho_{min} \leq \rho_e \leq 1 \end{cases} \end{cases}, \tag{3}$$

where $\bar{u}$ represents the displacement constraint. The problem is solved with the aid of a similar sensitivity analysis formulation, with the key difference that the required gradients are

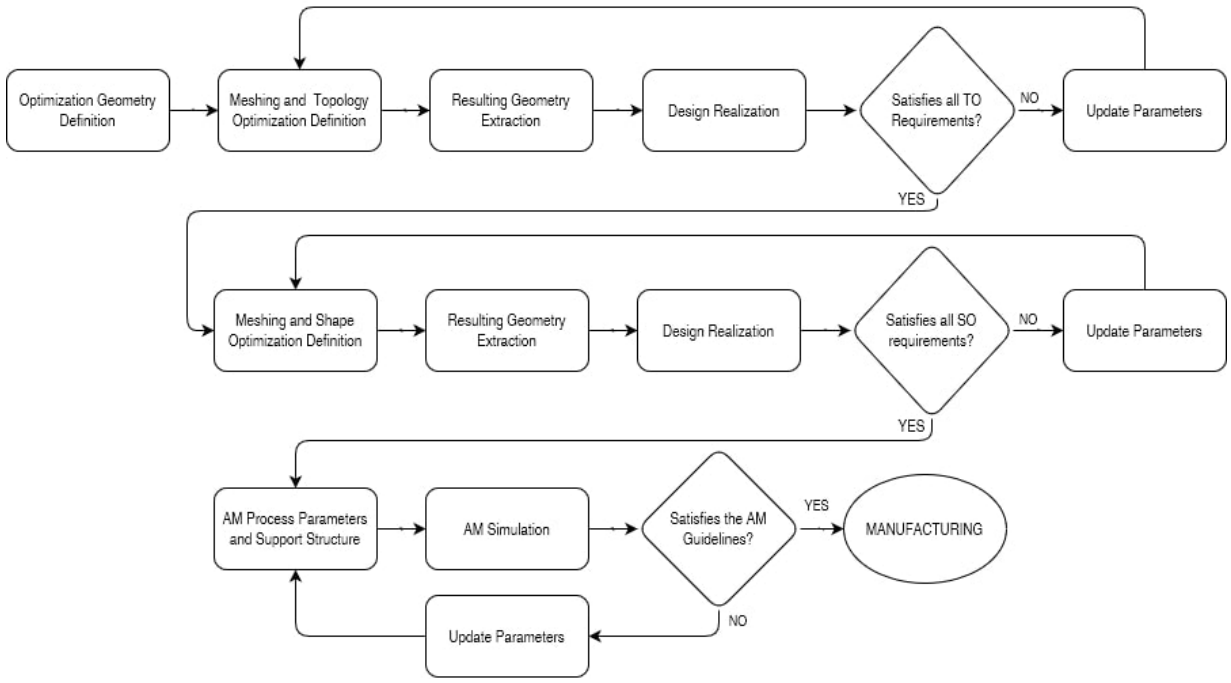

FIG. 2. Proposed design process workflow with DfAM considerations.

calculated on the constraints themselves ($\boldsymbol{u}(\boldsymbol{\rho})$), and not on the objective.

E. Shape optimization formulation

The shape optimization applied in this work is based on a non-parametric approach[16,17]. It is determined on implicit parameters, defined from the set of surface design nodes from the FE model, namely the displacement vector. The minimization of the maximum objective formulation is considered, in order to achieve overall higher robustness[15].

III. AM SIMULATION FORMULATION

The AM simulation problem is defined by the coupling between three main fields, the thermal, mechanical, and metallurgical. The metallurgical field, while important for example due to the dependence of distortion and residual stress on the solid phase transformations that occur, will have its implementation limited in the context of the present work, with the focus being on the thermal and mechanical problems. It can be stated that the plastic deformation induced friction heat is negligible, when compared to the thermal energy present in the system, leading to a weakly coupled or uncoupled model that is currently employed in most analyses[18–20].

A. Transient thermal problem formulation

The transient temperature distribution can be modeled by the heat equation,

$$\frac{\partial T}{\partial t} = \frac{k(T)}{c_P(T)\rho}\nabla^2 T + \frac{1}{c_P(T)\rho}\dot{Q}_v, \tag{4}$$

where T is the temperature field, $k(T)$ is the thermal conductivity, $c_P(T)$ is the specific heat, $\rho(T)$ is the density, and $\dot{Q}_v$ is the volumetric heat source term, that in this case is associated with the laser beam. Convection and radiation heat loss effects are defined at the free surfaces of the printed part and define the surface heat flux, $\dot{Q}_s$,

$$\dot{Q}_s = \dot{Q}_{convection} + \dot{Q}_{rad}, \tag{5}$$

where $\dot{Q}_{convection}$ and $\dot{Q}_{rad}$ define the heat flux contributions from convection and radiation, respectively. Heat loss through convection happens mainly through the shielding gas (used to prevent oxidation), and the convective heat flux is given by,

$$\dot{Q}_{convection} = h\,(T - T_\infty)\,, \tag{6}$$

where h is the convective heat transfer coefficient, and T_∞ is the ambient temperature in the AM machine chamber.

Heat loss due to radiation is also present, even in a vacuum chamber setting[21]. Its effect is given by,

$$\dot{Q}_{rad} = \varepsilon\sigma\left((T - T_{zero})^4 - (T_\infty - T_{zero})^4\right), \tag{7}$$

where ε is the emissivity, σ is the Stefan-Boltzmann constant and T_{zero} is the absolute zero in a given temperature scale.

B. Mechanical problem formulation

A quasi-static incremental analysis is the approach used to solve the non-linear mechanical analysis problem. The governing conservation equation (equilibrium) is expressed as,

$$\nabla \cdot \boldsymbol{\sigma} = 0, \tag{8}$$

with appropriate boundary conditions, where $\boldsymbol{\sigma}$ is the stress tensor. The constitutive model considering elasto-plastic behaviour is given by,

$$\boldsymbol{\sigma} = \boldsymbol{C}\boldsymbol{\epsilon}^e, \tag{9}$$

where $\boldsymbol{C}$ is the fourth-order material stiffness tensor, in the case of isotropic behavior, a function of the Young's modulus E and the Poisson's ratio ν, and $\boldsymbol{\epsilon}^e$ is the elastic strain tensor. The total strain tensor $\boldsymbol{\epsilon}$ consists on three terms, the elastic strain $\boldsymbol{\epsilon}^e$, the plastic strain $\boldsymbol{\epsilon}^p$, and the thermal strain $\boldsymbol{\epsilon}^{th}$[8], such that,

$$\boldsymbol{\epsilon} = \boldsymbol{\epsilon}^e + \boldsymbol{\epsilon}^p + \boldsymbol{\epsilon}^{th} = \frac{1}{2}\left[\nabla \boldsymbol{u} + (\nabla \boldsymbol{u})^T\right]. \tag{10}$$

The thermal strain, at a temperature T, is defined by the thermal expansion coefficient α, and the reference temperature T_0. It is given by,

$$\boldsymbol{\epsilon}^{th} = \alpha\,(T - T_0)\,\boldsymbol{\delta}_{ij}, \tag{11}$$

where $\boldsymbol{\delta}_{ij}$ is the Kronecker tensor.

IV. AM SIMULATION METHODOLOGY

The accurate modeling of the SLM process requires the definition and consideration of a set of process elements, these being the toolpath/scan path information, the progressive material deposition information, the thermal-structural material properties, and the laser/heat input properties. Software dedicated to AM simulation already exists and it is used. However, it is commonly associated with specific machines, resulting in license and data format limitations. In order to overcome this difficulty, both Abaqus with its built-in user subroutines and mesh intersection tools, and Autodesk Netfabb were utilized to define the scan path based on the AM machine printing parameters.

A. Toolpath-mesh intersection in Abaqus

The representation of both the laser source and the recoater roller is done through a toolpath. The main geometries of interest are the point and infinite line, respectively for the laser source and the recoater roller. However others can be considered for different applications, such as the box geometry, useful to characterize the material deposition in polymer extrusion or wire-feed methods.

1. Event series

The event series is a functionality in Abaqus that define time and space varying fields, independently of both the mesh and the simulation time increment. The field definition is done through a step function representation, linearly discretized in both space and time. Any event series has a fixed format set for both mandatory time and space definitions, to which a maximum of six user defined fields or dependent variables can be added.

Two event series are of particular interest in the simulation of the powder bed AM method, namely for the definition of the recoater roller motion, and the laser power, both defined in both time and space. The laser event series is used to define the laser power from which the heat flux can be calculated. On the other hand, the roller event series is used to progressively activate elements, and assumes a boolean dependent variable, equal to 1 when the roller is passing, and 0 otherwise.

2. Material deposition and progressive element activation

Progressive element activation in Abaqus is employed to simulate the material deposition event that occurs in powder bed-type AM processes, due to the layer-by-layer raw material deposition from each recoater roller passage, and it had been used previously[22,23], e.g. in the case of laser cladding[24,25].

The path taken by the roller is represented by an infinite line moving along the same direction as the roller, defining a plane parallel to the new layer, and perpendicular to the printing direction. Such infinite line intersects the finite element mesh, either partially or fully activating said elements.

3. Moving heat flux and progressive heating

The newly deposited layer of raw material is fused due to the passage of the heat source, characteristic of the AM process of interest (laser, electron beam, etc.). This makes the modeling of the heat source essential to properly define the AM process, mainly through its power, scan path, and heat distribution type.

B. Abaqus user subroutines

User subroutines are implemented to increase the capabilities of Abaqus to simulate the AM process[15]. Two particular subroutines are utilized to aid the simulation of both the moving heat flux and the progressive element activation process.

These are *UMDFLUX* and *UEPActivationVol*, and the respective accompanying data setup subroutines *UMDFLUXSetup*, and *UEPActivationSetup*.

UMDFLUXSetup provides the required data structures to the Mesh Intersection Tool, such as mesh and event series details related to the moving heat source at the start of the step. At the beginning of the increment it is once again called to compute the heat flux per element, based on the intersection between the event series laser path and the mesh.

UMDFLUX is responsible for the definition of the heat flux distribution of multiple moving heat sources, continuously with respect to time and space. The subroutine accounts for different heat source models, such as the Goldak heat source model[26] and the concentrated point energy source model. It allows for a continuous definition of one or more flux sources, that do not depend on the mesh and instead are based on the event series information. For each element, the subroutine obtains the total flux for each event provided by the Mesh intersection Tool during *UMDFLUXSetup*.

UEPActivationSetup, at the beginning of the step, creates and provides to the Mesh Intersection Tool the required data structures to perform the progressive element activation, with accordance to both the mesh and the recoater roller event series. On the other hand, at the start of the increment it triggers the Mesh Intersection Tool to compute the intersection between the recoater roller event series and the mesh for the specific increment time interval. The volume fractions are stored by the Mesh Intersection Tool.

UEPActivationVol obtains the volume fraction previously computed by *UEPActivationSetup* at the start of the increment for each element of interest. The volume fraction increase defines the partial element activation process.

The diagram in figure 3 highlights the order of interaction between the user subroutine calls and the mesh intersection tool during the Abaqus analysis.

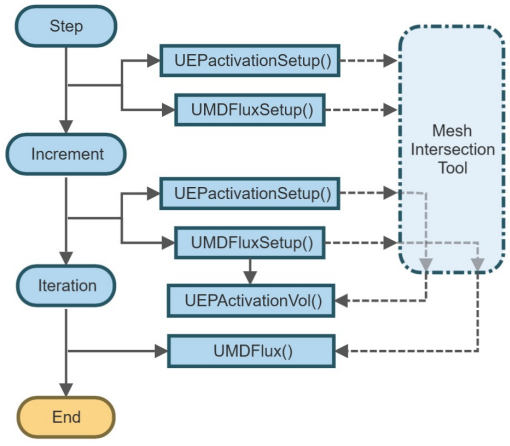

FIG. 3. Flowchart of an Abaqus AM simulation analysis, including the user subroutine calls and interactions with the mesh intersection tool. Based on the 2022 SIMULIA Abaqus documentation[15].

C. Abaqus AM modeler plug-in

The AM modeler plug-in is developed and made available by SIMULIA, with the main goal of aiding the definition of the necessary keywords that coordinate the extensive data needed by the user subroutines. It requires the previous definition of both thermal and structural models, both the heat source path and recoater roller event series, and the simulation parameters.

D. AM simulation geometry pre-processing

The geometry pre-processing process is divided into three major steps, these being, printing support design and generation, voxelization, and part slicing and scan path information.

With the CAD geometry of the part to be printed, firstly the supports need to be designed and generated alongside the part. This is done utilizing Autodesk Netfabb's automated tools. Following this procedure, the new mesh file is rasterized in order to create a voxelized representation of the part and supports. The result of the procedure is a regular hexahedral element based mesh, constructed along the printing direction. Finally, the resulting mesh can be exported as a STL file and imported again in a slicing software to obtain the scan part information.

1. *Voxelization and voxel-based meshing*

The voxelization of a continuous geometry consists on the discrete subdivision of such a geometry into cells or voxels. In the present case, each voxel is defined by the same geometry of a regular hexahedral finite element, and the volume fraction property. The volume fraction property is a scalar discrete field that characterizes the intersection between a continuous geometry (reference geometry) and a finite element mesh (intersection grid). Therefore, the part needed to define the voxelization process are,

- **Reference Geometry:** A CAD file of the part to be printed, which will be transformed to a voxel-based geometry;
- **Intersection Grid:** A hexahedral element-based mesh that bounds the reference geometry. The elements are oriented with respect to the printing direction, to mimic the progressive layer deposition and facilitate both the progressive element activation, and the heating of the elements from the moving heat flux.

From the description of the process, it is apparent that the quality of the geometrical approximation is dependent on the dimensions of the intersection grid. However, a higher resolution intersection grid warrants more computational resources, so a balance must be found such that important details are accurately captured, and the simulation is feasible to be ran in reasonable time according to available computational power.

Despite further comparisons between conventional meshing with tetrahedral elements, and voxel-based meshing with hexahedral elements being necessary, key features of both methods hold the following items apparent,

- The voxel-based mesh showcases an uniform meshing grid, that is built based on the progressive layer deposition characteristic of a powder bed AM process. Since the voxel-based mesh is constructed along the printing direction, each element is activated at a similar time and rate compared to it's neighboring elements in the layer plane, potentially improving convergence;
- The conventional mesh does a better job at representing the surface of the part, whereas the voxel-based one exhibits a jagged representation of curved surfaces, which can lead to stress concentration spots;
- The transformation to an adequately sized voxel-based mesh means less complexity and computational resources consumed;
- The likelihood of bad elements being present is reduced with the use of a voxel-based mesh, in spite of the geometrical complexity of the original part.

2. Part slicing and scan path information

With the aim of achieving a generalized workflow applicable to any machine parameters and complex geometry, it is firstly studied how to take advantage of Autodesk Netfabb's geometry slicing and support structures creation capabilities, as well as the AM process set-up, and import this information into FEM simulation, namely in Abaqus.

The slicing process depends on the geometry itself, part orientation, build direction and printing layer size, which are parameters Autodesk Netfabb allows to adjust. As these are set, the software proceeds to cut the tessellated triangles such that each layer is made up of closed polygons that constitute the cut surface. These closed perimeters are defined as walls or contours, whereas the inside region is the infill. The hatch filling geometry is defined through the set of parameters made available in Autodesk Netfabb and is automatically added to each layer.

Finally, with the entirety of the scan path defined geometrically, the speed of the laser and its power remain to be set. The parameters can be defined separately for both the contour and the infill, allowing to define the position of the laser both in space and time. The output of the slicing process is chosen to be the laser vector LSR file format.

E. Low-resolution thermo-mechanical simulation in Abaqus

As a first approach, and in order to achieve a computationally efficient simulation, a lower resolution simulation is proposed, using a coarser mesh (element size larger than a unitary printing layer thickness), a larger time increment and a concentrated moving heat source model. The larger time increment results in the lumping of the printing events, such that the near-field action is not accurately captured, but instead its effect is averaged, while the far-field region is still described.

1. Annealing effect

The annealing effect is a feature allowing to simulate the stress relaxation and creep processes that occur typically at temperatures higher than a so called relaxation temperature T_{relax}, to be determined. In this case, the stress and strain components are set to zero if the element temperature exceeds T_{relax}. This is important, because elements are activated at high temperature. In fact, as the time step of the low-resolution simulation is not enough to capture the high temperature peaks at the melting spot, an initial temperature is applied to each newly activated element, such that it defines the initial thermal contraction during the structural simulation, and so a proper constitutive description at high temperature is needed. As such, the value chosen for the present work for Ti-6Al-4V, T_{relax} = 690ºC, taken from literature[27].

F. Thermal simulation definition

The uncoupled thermal-mechanical simulation is started by the definition of the thermal history of the process. The approach taken in this work focuses on a transient thermal analysis, with a duration longer than the one of the printing of the part itself, to allow for part cooling.

1. Cooling effects

Progressive cooling is present throughout the entire building process, namely through both convection and radiation effects. Heat loss due to radiation is defined by the ambient temperature, T_{amb}, inside the printing chamber, as well as the emissivity of the exposed surface of the part, ε. On the other hand, heat loss through convection also takes places, with the key-parameter heat transfer or film coefficient, h. It is defined according to the inert gas atmosphere present in the printing chamber (typically the inert gas Argon).

Partial element activation adds heat content to the system, and also plays a role on the cooling effects due to both convection and radiation, as it allows to change the exposed surfaces of the elements cut by the activation plane.

2. Initial and boundary conditions

Both the initial and boundary conditions are essential to accurately represent the temperature evolution of the part during printing. In order to define substrate process heating, a fixed temperature boundary condition is applied to the bottom

of the build plate part T_{sub}. Separately, the powder bed preheating effect is defined by a predefined field applied to the entire build plate in the initial step, named T_{pre}.

The initial temperature of the deposited powder from each printing layer, T_{part}, is also set through a pre-defined field applied to the printing part.

G. Mechanical simulation definition

The mechanical field is driven by the results of the thermal simulation. The same laser-path and recoater roller event series INP files are needed, in order to properly activate the elements, and the temperature field information stored in the thermal simulation ODB file is also required. Similarly, for numerical simplicity, the same mesh geometry is shared between the thermal and structural simulations, with the sole difference being the transformation of heat transfer elements into general 3D solid elements.

1. Initial and boundary conditions

Under a low-resolution assumption, there is the need to define the initial temperature of elements as they're activated, as the relaxation temperature, T_{relax}, during the structural analysis.

To prevent rigid body motion, the displacement constraints are applied to the building plate. The building part itself is then defined through the tie constraint connection with the building plate. Finally, the results of the thermal simulation are introduced through a predefined field, which makes use of the ODB file generated by the thermal analysis.

V. AMATHO TOPOLOGY OPTIMIZATION RESULTS

For the topology optimization procedure, the load application points are connected to each of the six respective mounting bosses through structural distributing coupling constraints, such that relative motion between each is possible. Identically, the centers of mass are connected to the same mounting bosses through a continuum distributing coupling constraint (see figure 4).

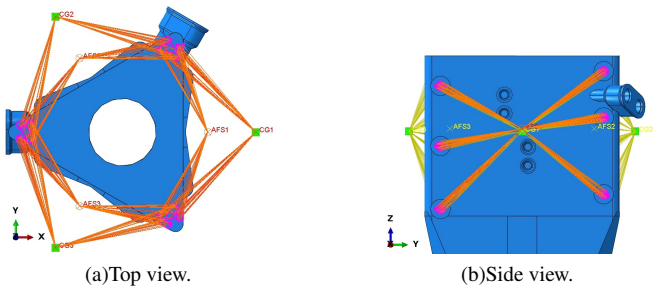

(a)Top view. (b)Side view.

FIG. 4. Connection between the load application point and center of gravity, and the 6 mounting bosses.

The bolt holes at the bottom region are used to apply the boundary conditions to the component. The bolt hole displacement constrained in the x and y directions (figure 5(a)), the top and underside bolt hole regions displacement constrained in the z direction (figure 5(b)), and the fillet feature on the conic element displacement constrained in the x and y directions (figure 5(c)).

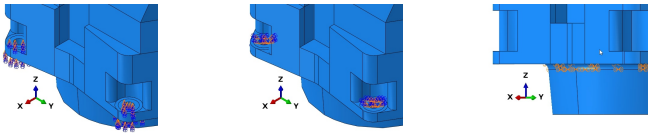

(a)Bolt hole cylinder. (b)Top and underside of bolt hole. (c)Connecting fillet region.

FIG. 5. Bracket boundary conditions.

The load cases considered are purely related to the proof stress loading, such that the Ti6Al4V ELI Titanium Alloy linear-elastic properties can be used throughout all topology optimization simulations.

A. AMATHO topology optimization setup

Leonardo Helicopters provided both the design envelope and fixed elements CAD files. The design envelope defines the volume subject to optimization and changes, whereas the fixed elements represent mounting regions to other helicopter components and parts, and shall remain unchanged. However, Leonardo accepted changes that were carried out to the fixed elements region to mend broken or missing regions (since the provided file was obtained directly from the current component which has bolts connecting the two parts), to include the central hydraulic region (as its optimization is beyond the scope of this work, and therefore remains identical), and to simplify the geometry to reduce the need for a fine mesh (see figure 6(a), where red regions highlight removed material, and green regions added material). Such changes are thereafter used to update the design envelope (see figure 6(b)). The assembly of the parts is meshed with quadratic tetrahedron elements (C3D10), and an element size of 7mm.

A volume minimization approach is considered with displacement and frequency constraints, utilizing both SIMP and MIMP interpolation methods. The stiffness requirements are approximated to the displacement limits based on the loading at each point (axial stiffness and normal stiffness) or pair of points (relative stiffness). Several trial cases are defined to better understand the implementation of topology optimization to the part geometry, and the impact of the parameters on the final design solution. More precisely, SIMP and MIMP methods are compared in trial cases 1 to 4, whereas trial case 5 marks the introduction of the numerous relative and normal stiffness constraints. Trial case 1 (figure 7(a)) is defined by a volume minimization topology optimization task, with axial displacement constraints, utilizing SIMP, whereas trial case 2 (figure 7(b)) utilizes MIMP. Both solutions are iden-

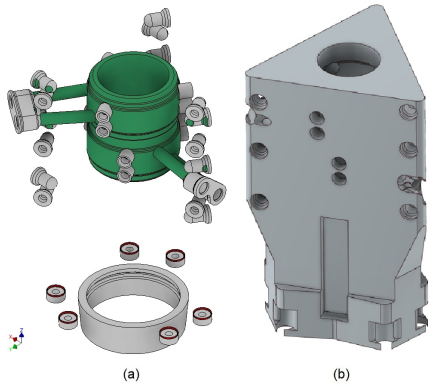

FIG. 6. Optimization individual components. (a) Fixed elements. (b) Design envelope.

tical, since no mass related design response is implemented, with trial case 1 showcasing a lower number of gray elements (with relative density between 20% to 80%).

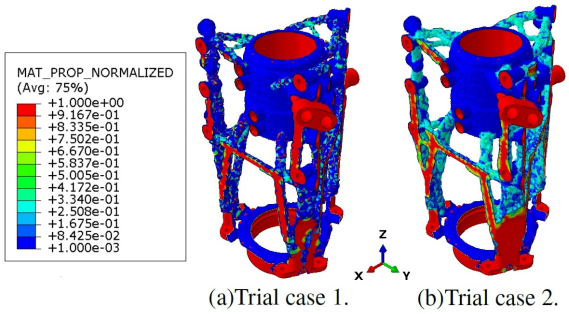

FIG. 7. Trial cases 1 and 2 normalized material property results.

Trial case 3 (figure 8(a)) is the same as trial case 1, with the added inclusion of the minimum frequency constraint. Similarly, the trial case 4 (figure 8(b)) is the same as trial case 2, with the added inclusion of the minimum frequency constraint. The introduction of the frequency design response drives both trial cases to different solutions. In fact, trial case 3 fails to achieve convergence, while trial case 4 converges to a well-connected design that also respects the frequency constraint.

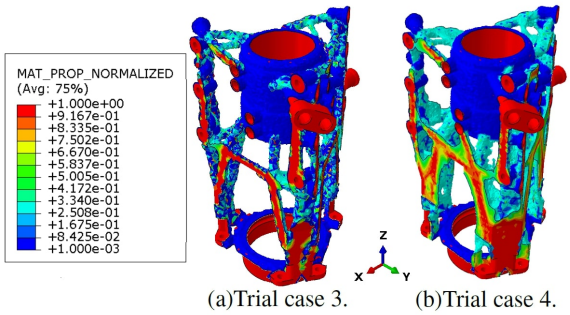

FIG. 8. Trial cases 3 and 4 normalized material property results.

A smoothing process is done by Tosca Structure.smooth, so the STL resulting file can be interpreted in Altair Inspire using polyNURBs and turned into a solid part to be validated in Abaqus under the same loading and boundary conditions. A summary of the relative mass and frequency can be seen in table I, revealing the inability of the SIMP method to comply with the frequency requirement. All interpreted designs have a mass lower than the current geometry. Additionally, all trial cases respect the axial stiffness requirements.

TABLE I. Trial cases 1, 2, 3, and 4 mass and frequency response results.

Trial case	Mass	Frequency
1	0.8456	0.6847
2	0.8766	0.6953
3	0.8556	0.7188
4	0.9410	1.2524

An additional trial case is introduced with the inclusion of the relative and normal stiffness constraints in the form of displacement design responses. Since the trial case 4 is the only one to satisfy the frequency constraint, it is chosen to be the trial case to expand on with the new constraint. In fact, the newly obtained design is vastly different, with a frame truss-like structure connecting the outermost mounting bosses in each face. The interpreted final design can be seen meshed in figure 9. It respects both the axial stiffness and frequency constraints, while having a vastly superior performance with regards to the relative and normal stiffness constraints when compared to the trial case 4 design. It also has a similar mass at 0.9771 of the current design. Therefore, it is the chosen topology optimized design.

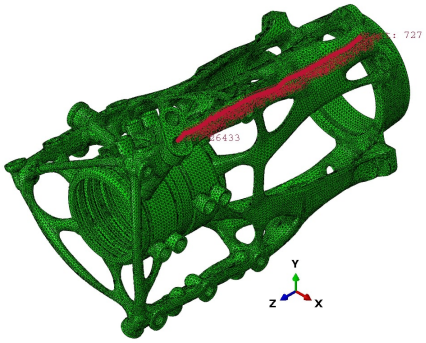

FIG. 9. Meshed trial case 5 interpreted design. The path for the Von Mises stress plots is highlighted.

VI. AMATHO SHAPE OPTIMIZATION RESULTS

One of the main aims of the present study is to minimize and homogenize stress hotspots that occur during static analysis. Additionally, the proof stress loading case is considered, and not the ultimate stress, as the behavior of the component above fracture failure is not accurately modeled with the type

of elements that were considered. The shape optimization task utilizes the controller based optimality criteria to perform a Von Mises stress maximum minimization, considering the same load cases as in the topology optimization task. The optimization constraint is defined as a constant volume. The results of the shape optimization process can be seen in figure 10, where the surface displacement vector is represented. Regions in red expand outwardly, and blue regions inwards.

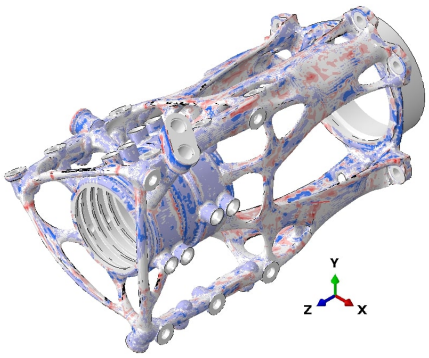

FIG. 10. Shape optimization results, namely the surface vector.

Based on said surface vector results, the polyNURBs file referring to trial case 4 is modified. The first iteration results in a 1% mass decrease, and smoothing out of the Von Mises stress, as seen in figures 11 referring to the red path highlighted in figure 9.

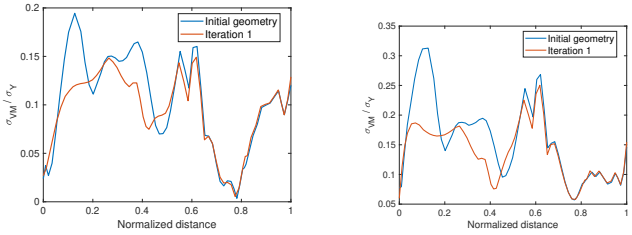

(a)Axial load case. (b)Bending 1 load case.

FIG. 11. Normalized path Von Mises stress results comparison between initial, and iteration 1 geometries.

An additional iteration is performed to further reduce the weight of the component, while maintaining the stress homogeneity, and ensuring it complies with the design requirements. In fact, a final mass reduction of 5.12% is achieved compared to the current component design, while respecting the proposed design requirements.

The resulting geometry from the applied structural optimization process is seen in figures 12, and 13, where the stress, and displacement magnitude fields are shown, respectively, and compared to the current component performance counterpart. The results are obtained for proof stress loading case under bending. It should also be noted that the scale utilized is entirely identical between the two components (omitted).

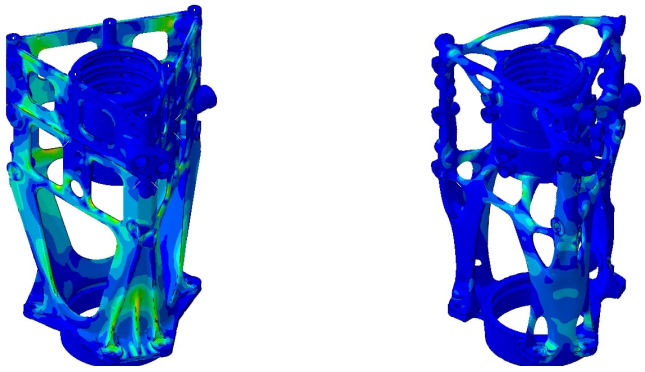

(a)Current design. (b)Proposed design.

FIG. 12. Von Mises stress results comparison under proof bending 1 load case.

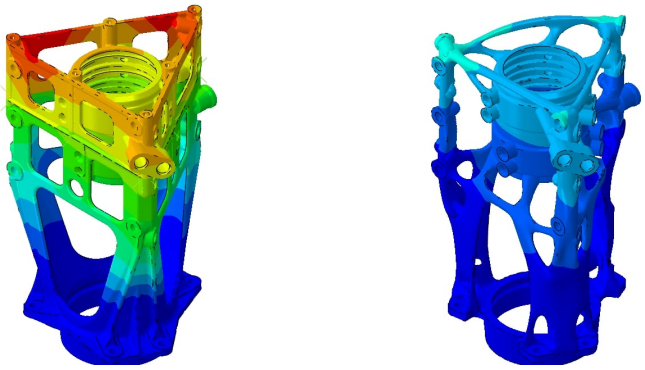

(a)Current design. (b)Proposed design.

FIG. 13. Displacement magnitude results comparison under proof bending 1 load case.

VII. AMATHO AM SIMULATION RESULTS

A low-resolution AM process simulation is implemented on a scaled version of the part to verify the printability of the proposed design, following the implementation of a benchmarking simulation that validates the chosen method, utilizing a model defined by the National Institute of Standards and Technology (NIST) (see Appendix A). Additionally, for consistency with said simulation, the same temperature field boundary conditions are applied. The substrate is pre-heated to a temperature of 80ºC, and the newly deposited layer is at a temperature of 40ºC, the same as the surrounding environment temperature. The first step involves the definition of the support structures in Autodesk Netfabb utilizing its automated creation tools. These depend on the printing process itself. A regular hexagonal bar support was chosen and it is shown in figure 14(a).

The voxelization process, in addition to the surface mesh describing the part to voxelize, requires the creation of the intersection grid, a hexahedral element-based mesh "box" that encapsulates the part. A grid with element size 0.4mm is defined, such that each element contains, approximately, 7 physical layers. Finally, the part intersection translates to the defi-

nition of a volume fraction in the grid elements. The ones with a value higher than 0 (intersection took place) are extracted and translated into an INP file. The INP file characterizes the node and element sets which allow for the definition of a solid mesh in Abaqus (see figure 14(b)).

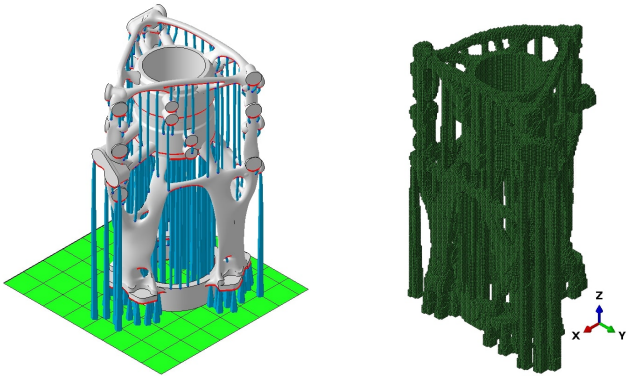

(a)Bracket with support structure (in blue).

(b)Voxel-based geometry.

FIG. 14. AM simulation geometry pre-processing steps.

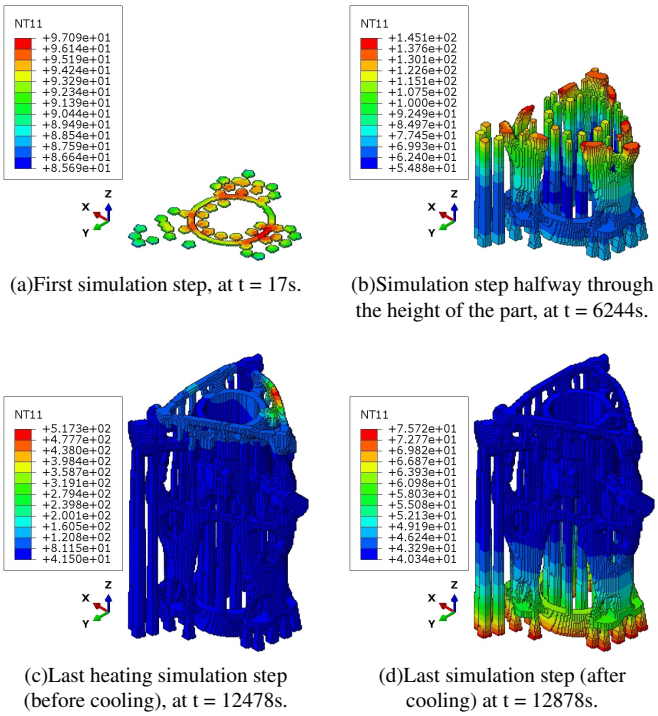

(a)First simulation step, at t = 17s.

(b)Simulation step halfway through the height of the part, at t = 6244s.

(c)Last heating simulation step (before cooling), at t = 12478s.

(d)Last simulation step (after cooling) at t = 12878s.

FIG. 15. Results of the AM process thermal simulation applied to the aerospace component.

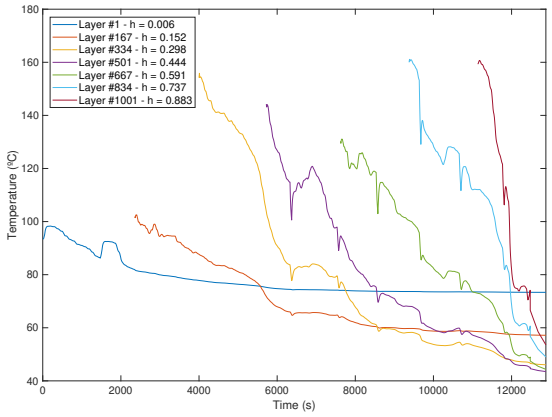

FIG. 16. Temperature evolution (in ºC) of 7 different nodes at increasing relative heights.

A. Thermal simulation results

The temperature field drives the mechanical analysis in the proposed AM simulation. The snapshots from the transient thermal simulation represent the moment the new layer deposition occurs (described in subsection IV E). Examples of these can be seen in figure 15(a) (representing the first physical layer), figure 15(b) (representing a half-way through physical layer), figure 15(c) (representing the last physical layer), and figure 15(d) (representing the moment after the post-printing cooling interval). The peak temperatures are not as high as expected from a fine time increment simulation. However, the top part (last printed layer), converges to approximately 40ºC, the temperature of the surrounding environment, whereas the bottom part (first printed layer) converges to approximately 80ºC, the temperature of the substrate.

The temperature plot with respect to time can be seen in figure 16, showcasing the nodal temperature (NT11) of chosen nodes, calculated as moving averages (Eulerian reference frame), from the first printed layer to the last.

B. Mechanical simulation results

The results of the mechanical simulation reveal high distortion in a region with overhanging material and no support structure, as it is expected (see figure 17).

The representation of the residual stress is done with the Von Mises stress distribution (depicted in figure 18). However, the low-resolution nature of the simulation has its drawbacks revealed in the stress distribution, namely the presence of stress concentration points at the surface of the part, as a result of the voxelization process, that causes sharp corners at the part's surface. The region is, as expected, subjected to larger temperature gradients due to the close contact to the cooler elements, such as the inert gas. While displacement is less susceptible to mesh changes, the stress field showcases larger sensitivity, leading to the observed stress peaks at single nodes. Nevertheless, the stress distribution is, for the most part, fairly homogeneous.

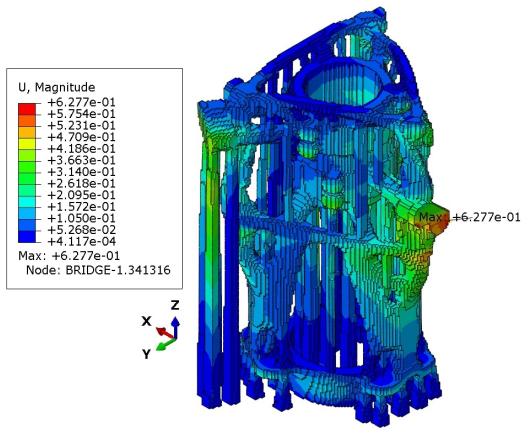

FIG. 17. Displacement results (in mm) of the AM process simulation applied to the aerospace component.

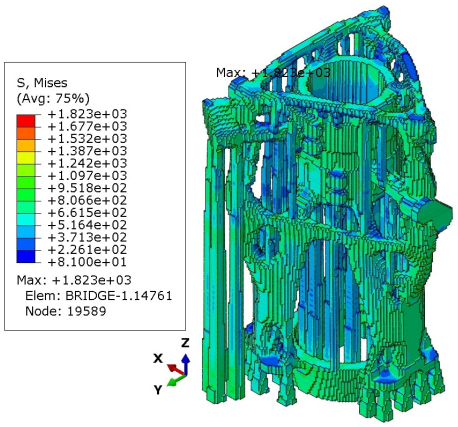

FIG. 18. Von Mises stress (in MPa) results of the AM process simulation applied to the bracket component.

VIII. DISCUSSION AND CONCLUSIONS

It has been shown that the MIMP interpolation method, while based off the SIMP method, achieves both convergence, and better results for the given design constraints. In fact, a mass dependent analysis benefits from the use of MIMP, which is in fact verifiable. Comparing the results from trial cases 1 and 2, both volume minimization problems with displacement constraints, they exhibit the same geometry result, except for the increase of gray elements in trial case 2 (from 1.32% with SIMP, to 3.97 with MIMP). Considering that the design interpretation is at the discretion of the user, the proposed solution being similar at a grand scale, it means that both can be designed the same way. However, the introduction of the frequency constraint in trial cases 3 and 4 highlights the differences between both interpolation methods. As SIMP fails to achieve convergence and the frequency constraint oscillates throughout the optimization process, MIMP converges with fair swiftness. By comparing all results, MIMP is chosen to be the interpolation method to be used for the remaining trial cases.

The introduction of further design constraints in the optimization task results in definite geometrical changes, namely in trial case 5, which features a frame surrounding each face, in order to comply with relative displacement constraints between mounting bolts. Considering this, and the final mass savings of 2.29% the original component, trial case 4 is deemed the best design and the one to undergo further analysis. Shape optimization compliments the design process by addressing another set of design requirements, namely the ones pertaining to static strength. The final design represents a 5.12% mass decrease compared to the current component. Such reduction is largely attributed to the DfAM methodology employed, as it allows for a single component design, not limited to typical manufacturing constraints that do not allow for *organic-looking* designs as the one presented.

The obtained thermal field in the aerospace part follows the predicted behavior based on the two driving effects, these being the fact that as the printed part height increases, the influence of heat conduction to the substrate decreases, leading to a tendency to increase the temperature, seen between layers 1, 167, and 334; and the increasing effect of convection and radiation cooling effects. The superposition of the two effects leads to the initial increase of the temperature per layer, followed by a plateau and eventual decrease. Moreover, the voxelization process with such a complex geometry implies initialization of layers with vastly different sections and number of elements on after the other, leading to the discontinuities present in figure 16, as the heat stored for each step can be vastly different.

The results obtained from the AM simulation reveal distortion which is in fact higher in regions with unsupported overhanging material, as expected, reaching a maximum of 0.6277mm.

Combination of Topology and Shape Optimization with Finite Element Modeling can be a powerful tool in the design of aerospace components produced by Laser Based Additive Manufacturing. This can be achieved namely by combining the mass reduction and stress/distortion minimization capabilities of Optimization algorithms, with the predictive power of the Finite Element Method to describe thermal and residual stress fields, in what concerns the production of such components by means of Laser Based Additive Manufacturing.

ACKNOWLEDGMENTS

This paper is in memory of Professor Jyoti Mazumder, a pioneer in Laser Deposition Methods and Additive Manufacturing of Metals, as well as countless contributions to the fields of Laser Materials Processing and Laser Based Diagnostics.

The project leading to this application has received funding from the Clean Sky 2 Joint Undertaking (JU) under grant agreement No 717194 (AMATHO). The JU receives support from the European Union's Horizon 2020 research and innovation programme and the Clean Sky 2 JU members other than the Union. A. M. Grande and G. Sala are grateful to S. Sartori and F. Montagna (Leonardo Helicopters) for the provided design data and for the helpful discussions.

J. M. Guedes was partially supported by LAETA project UIDB/50022/2020.

A.M. Deus was partially supported by CeFEMA project UIDB/04540/2020. Both projects are sponsored by FCT, the Portuguese Agency for Science and Technology.

DATA AVAILABILITY STATEMENT

The data that support the findings of this study are available from Leonardo Helicopters. Restrictions apply to the availability of these data, which were used under license for this study. Data are available from the authors upon reasonable request and with the permission of Leonardo Helicopters.

[1] J. Beaman, "Historical perspective," JTECIWTEC Panel Report on Rapid Prototyping in Europe and Japan , 737–760 (1997).

[2] D. L. Bourella, J. J. Beaman, M. C. Leub, and D. W. Rosenc, "History of additive manufacturing and the 2009 roadmap for additive manufacturing : Looking back and looking ahead," (2009).

[3] S. S. D. D. T. Pham, *Rapid Manufacturing The Technologies and Applications of Rapid Prototyping and Rapid Tooling* (Springer, 2001).

[4] P. A. L. Ciraud, "Method and device for manufacturing any articles from any meltable material - de2263777a1 patent," `https://patents.google.com/patent/DE2263777A1/en`, [Online; accessed April 2022].

[5] W. Associates, "Wohlers report 2021," `https://wohlersassociates.com/2021report.htm`, [Online; accessed April 2022].

[6] T. Nakagawa, "Blanking tool by stacked bainite steel plates," Press Technique , 93–101 (1979).

[7] M. K. Thompson, G. Moroni, T. Vaneker, G. Fadel, R. I. Campbell, I. Gibson, A. Bernard, J. Schulz, P. Graf, B. Ahuja, and F. Martina, "Design for additive manufacturing: Trends, opportunities, considerations, and constraints," CIRP Annals **65**, 737–760 (2016).

[8] S. Chen, *Investigation of FEM numerical simulation for the process of metal additive manufacturing in macro scale*, Ph.D. thesis (2019).

[9] C. Guo, W. Ge, and F. Lin, "Effects of scanning parameters on material deposition during electron beam selective melting of ti-6al-4v powder," Journal of Materials Processing Technology **217**, 148–157 (2015).

[10] M. P. Bendsøe and N. Kikuchi, "Generating optimal topologies in structural design using a homogenization method," Computer Methods in Applied Mechanics and Engineering **71**, 197–224 (1988).

[11] R. Ferreira, *Comprehensive Design Methodology for Metal Aeronautical Components Produced by Additive Manufacturing*, Master's thesis, Politecnico di Milano (2022).

[12] M. Bendsøe and O. Sigmund, *Topology Optimization: Theory, Methods, and Applications* (Springer Berlin Heidelberg, 2003).

[13] F. Goetz, "Simulia update release 2021 news in tosca, isight and fe-safe," `https://events.3ds.com/simulia-update-release-\\2021-news-tosca-isight-and-fe-safe`, [Online; accessed April 2022].

[14] G. I. N. Rozvany, M. Zhou, and T. Birker, "Generalized shape optimization without homogenization," Structural Optimization **4**, 250–252 (1992).

[15] Dassault Systèmes, "Simulia user assistance online," (2022), [Online; accessed April 2022].

[16] R. Larsson, *Methodology for Topology and Shape Optimization: Application to a Rear Lower Control Arm*, Master's thesis, Chalmers University of Tecnhology (2016).

[17] R. Meske, J. Sauter, and E. Schnack, "Nonparametric gradient-less shape optimization for real-world applications," Structural and Multidisciplinary Optimization **30**, 201–218 (2005).

[18] B. Cheng, S. Shrestha, and K. Chou, "Stress and deformation evaluations of scanning strategy effect in selective laser melting," Additive Manufacturing (2016).

[19] M. Zain-ul abdein, D. Nelias, J.-F. Jullien, and D. Deloison, "Prediction of laser beam welding-induced distortions and residual stresses by numerical simulation for aeronautic application," Journal of Materials Processing Technology **209**, 2907–2917 (2009).

[20] F. Kong and R. Kovacevic, "3d finite element modeling of the thermally induced residual stress in the hybrid laser/arc welding of lap joint," Journal of Materials Processing Technology - J MATER PROCESS TECHNOL **210**, 941–950 (2010).

[21] W. Sames, F. List, S. Pannala, R. Dehoff, and S. Babu, "The metallurgy and processing science of metal additive manufacturing," International Materials Reviews **61**, 1–46 (2016).

[22] P. K. Tekriwal and J. Mazumder, "Finite element analysis of three-dimensional transient heat transfer in gma welding," Welding Journal **67**, 150–156 (1988).

[23] P. K. Tekriwal and J. Mazumder, "Transient and residual thermal strain-stress analysis of gmaw," Journal of Engineering Materials and Technology, Trans. ASME **113**, 336–343 (1991).

[24] A. M. Deus and J. Mazumder, "Three-dimensional finite element models for the calculation of temperature and residual stress fields in laser cladding," ICALEO 2006-25th International Congress on Applications of Lasers and Electro-Optics, Laser Materials Processing Conference, Laser Institute of America, Orlando, Florida , 496–505 (2006).

[25] L. Costa, R. Vilar, T. Reti, and A. M. Deus, "Rapid tooling by laser powder deposition: Process simulation using finite element analysis," Acta Materialia **53**, 3987–3999 (2005).

[26] J. A. Goldak, A. P. Chakravarti, and M. Bibby, "A new finite element model for welding heat sources," Metallurgical Transactions B **15**, 299–305 (1984).

[27] E. R. Denlinger, J. C. Heigel, and P. Michaleris, "Residual stress and distortion modeling of electron beam direct manufacturing ti-6al-4v," Proceedings of the Institution of Mechanical Engineers, Part B: Journal of Engineering Manufacture **229**, 1803–1813 (2015).

[28] National Institute of Standards and Technology, "2018 am-bench test descriptions for amb2018-01," `https://www.nist.gov/ambench/amb2018-01-description` (2018), [Online; accessed April 2022].

[29] Y. Yang, M. Allen, T. London, and V. Oancea, "Residual strain predictions for a powder bed fusion inconel 625 single cantilever part," Integrating Materials and Manufacturing Innovation **8**, 294–304 (2019).

Appendix A: AM NIST benchmarking simulation in Abaqus

The AM simulation is implemented in Abaqus, by addressing AMB2018-01 Additive Manufacturing benchmark problem defined by NIST[28], such that the methodology implemented here is validated, to be later used in the part featured in the present study (see section VII). Built-in user subroutines and mesh intersection tools are utilized to define both the moving heat flux /laser source, and the progressive material deposition performed by the recoater roller in powder bed-type AM processes.

The benchmarking simulation geometry is made available as an STL file in the NIST website[28], as seen in figure 19.

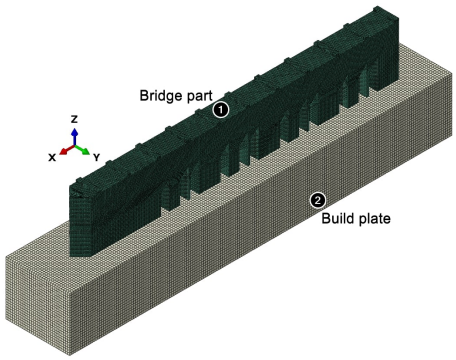

FIG. 19. Meshed geometries of the NIST bridge and build plate[29].

1. AM benchmark results

The residual elastic strain and distortion results are compared against the x-ray diffraction measurements provided by NIST, 2018[28]. Namely, the z and x direction residual elastic strains are obtained at the $y = 2.5$mm middle cross-section of the printed part. Figures 20(a) and 21(a) present the residual elastic strain in the x and z-directions, respectively. The residual elastic strain in the x and z-directions provided by NIST, 2018[28] can be seen in figures 20(b) and 21(b), respectively.

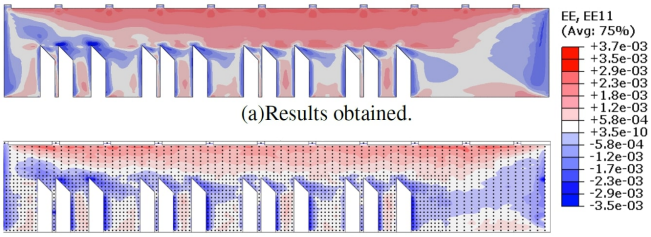

(a)Results obtained.

(b)Benchmark experimental results.

FIG. 20. Residual elastic strain in the x-direction.

Additionally, elastic strain in the z-direction path data at $z = 2.75$mm (figure 22(a)) and $z = 10.75$mm (figure 22(b)), both at $y = 2.5$mm, are compared against the NIST benchmark test data. The obtained results show a good correlation with the tests, at both build heights.

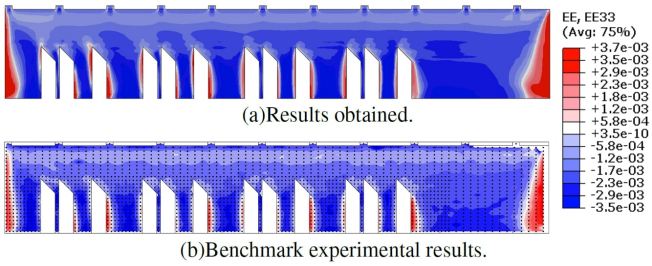

(a)Results obtained.

(b)Benchmark experimental results.

FIG. 21. Residual elastic strain in the x-direction.

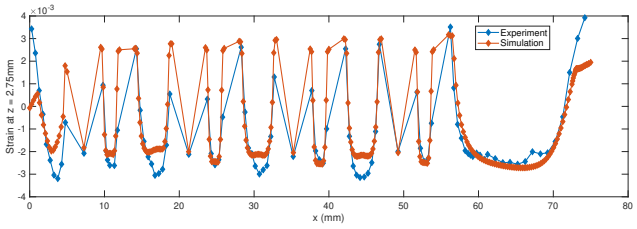

(a)z = 2.75mm.

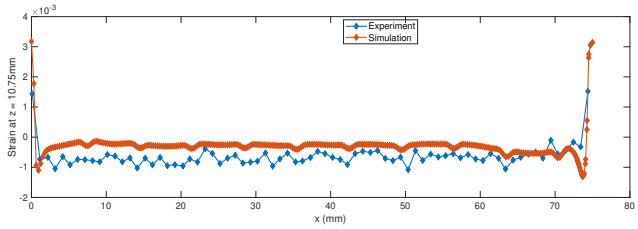

(b)z = 10.75mm.

FIG. 22. Path z-direction strain measured at two different heights.

Finally, distortion is measured at the eleven top ridges found on the part, at $z = 12.5$mm in the central plane at $y = 2.5$mm. The plot in figure 23 shows both the benchmark test results and simulation results obtained, again suggesting a reasonably accurate prediction of the part behavior under AM printing conditions.

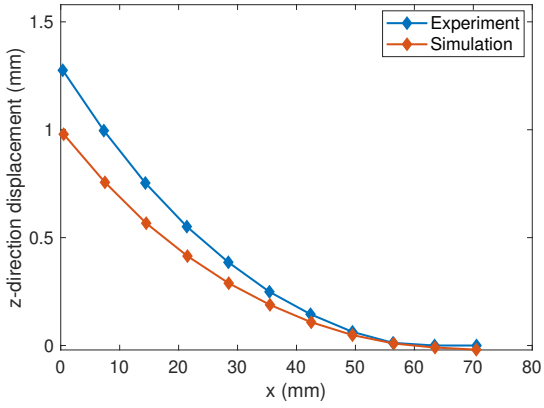

FIG. 23. Deflection measured that the part's top ridges.